Achieving hard X-ray nanofocusing using a wedged multilayer Laue lens

Xiaojing Huang,[1] Raymond Conley,[1,2] Nathalie Bouet,[1] Juan Zhou,[1] Albert Macrander,[2] Jorg Maser,[2] Hanfei Yan,[1,*] Evgeny Nazaretski,[1] Kenneth Lauer,[1] Ross Harder,[2] Ian K. Robinson,[3,4] Sebastian Kalbfleisch[1] and Yong S. Chu[1]

[1] *National Synchrotron Light Source II, Brookhaven National Laboratory, Upton, NY 11973, USA*
[2] *Advanced Photon Source, Argonne National Laboratory, Argonne, IL 60439, USA*
[3] *London Centre for Nanotechnology, University College London, London, WC1H 0AH, UK*
[4] *Research Complex at Harwell, Didcot, Oxfordshire OX11 0DE, UK*

**hyan@bnl.gov*

Abstract: We report on the fabrication and the characterization of a wedged multilayer Laue lens for x-ray nanofocusing. The lens was fabricated using a sputtering deposition technique, in which a specially designed mask was employed to introduce a thickness gradient in the lateral direction of the multilayer. X-ray characterization shows an efficiency of 27% and a focus size of 26 nm at 14.6 keV, in a good agreement with theoretical calculations. These results indicate that the desired wedging is achieved in the fabricated structure. We anticipate that continuous development on wedged MLLs will advance x-ray nanofocusing optics to new frontiers and enrich capabilities and opportunities for hard X-ray microscopy.

OCIS codes: (340.0340) X-ray optics; (310.1860) Deposition and fabrication; (100.5070) Phase retrieval; (110.3010) Image reconstruction techniques.

References and links

1. H. Yan, R. Conley, N. Bouet, and Y. Chu, "Hard x-ray nanofocusing by multilayer Laue lenses," J. Phys. D: Appl. Phys. **47**, 263001 (2014).
2. J. Kirz, "Phase zone plates for x rays and the extreme UV," J. Opt. Soc. Am. **64**, 301–309 (1974).
3. S.-R. Wu, Y. Hwu, and G. Margaritondo, "Hard-x-ray zone plates: recent progress," Materials **5**, 1752–1773 (2012).
4. J. Maser, G. B. Stephenson, S. Vogt, W. Yun, A. Macrander, H. C. Kang, C. Liu, and R. Conley, "Multilayer Laue lenses as high-resolution x-ray optics," Proc. SPIE **5539**, 185–194 (2004).
5. H. Kang, J. Maser, G. B. Stephenson, C. Liu, R. Conley, A. T. Macrander, and S. Vogt, "Nanometer linear focusing of hard x-rays by a multilayer Laue lens," Phys. Rev. Lett. **96**, 127401 (2006).
6. H. Kang, H. Yan, R. Winarski, M. Holt, J. Maser, C. Liu, R. Conley, S. Vogt, A. Macrander, and G. B. Stephenson, "Focusing of hard x-rays to 16 nanometers with a multilayer Laue lens," Appl. Phys. Lett. **92**, 221114 (2008).
7. H. Yan, V. Rose, D. Shu, E. Lima, H. Kang, R. Conley, C. Liu, N. Jahedi, A. Macrander, G. Stephenson, M. Holt, Y. Chu, M. Lu, and J. Maser, "Two dimensional hardx-ray nanofocusing with crossed multilayer Laue lenses," Opt. Express **19**(16), 15069–15076 (2011).
8. X. Huang, H. Yan, E. Nazaretski R. Conley, N. Bouet, J. Zhou, K. Lauer, L. Li, D. Eom, D. Legnini, R. Harder, I. Robinson, and Y. Chu, "11 nm hard X-ray focus from a large-aperture multilayer Laue lens," Sci. Rep. **3**, 3562 (2013).
9. C. Liu, R. Conley, A. T. Macrander, J. Maser, H. C. Kang, M. A. Zurbuchen, and G. B. Stephenson, "Depth-graded multilayers for application in transmission geometry as linear zone plates," J. Appl. Phys. **98**, 113519 (2005).

#233519 - $15.00 USD Received 29 Jan 2015; revised 27 Mar 2015; accepted 29 Mar 2015; published 4 May 2015

10. T. Koyama, S. Ichimaru, T. Tsuji, H. Takano, Y. Kagoshima, T. Ohchi, and H. Takenaka, "Optical properties of MoSi2/Si multilayer Laue lens as nanometer x-ray focusing device," Appl. Phys. Express **1**, 117003 (208).
11. T. Liese, V. Radisch, and H. U. Krebs, "Fabrication of multilayer Laue lenses by a combination of pulsed laser deposition and focused ion beam," Rev. Sci. Instrum., **81**, 073710 (2010).
12. S. Braun, A. Kubec, M. Menzel, S. Niese, P. Kruger, F. Seiboth, J. Patommel, and C. Schroer, "Multilayer Laue lenses with focal length of 10 mm," J. Phys.: Conf. Ser. **425**, 052019 (2013).
13. T. Koyama, H. Takano, S. Konishi, T. Tsuji, H. Takenaka, S. Ichimaru, T. Ohchi, and Y. Kagoshima, "Circular multilayer zone plate for high-energy x-ray nano-imaging," Rev. Sci. Instrum. **83**, 013705 (2012).
14. F. Doring, A. Robisch, C. Eberl, M. Osterhoff, A. Ruhlandt, T. Liese, F. Schlenkrich, S. Hoffmann, M. Bartels, T. Salditt, and H. Krebs, "Sub-5 nm hard x-ray point focusing by a combined KirkpatrickBaez mirror and multilayer zone plate," Opt. Express **21**, 19311–19323 (2013).
15. M. Mayer, K. Keskinbora, C. Grevent, A. Szeghalmi, M. Knez, M. Weigand, A. Snigirev, I. Snigireva, and G. Schutz, "Efficient focusing of 8 keV x-rays with multilayer Fresnel zone plates fabricated by atomic layer deposition and focused ion beam milling," J. Synchrotron Rad. **20**, 433–440 (2013).
16. S. Niese, P. Krueger, A. Kubec, S. Braun, J. Patommel, C. G. Schroer, A. Leson, and E. Zschech, "Full-field X-ray microscopy with crossed partial multilayer Laue lenses," Opt. Express **22**, 20008–20013 (2014).
17. H. Yan, Y. S. Chu, J. Maser, E. Nazaretski, J. Kim, H. Kang, J. Lombardo, and W. Chiu, "Quantitative x-ray phase imaging at the nanoscale by multilayer Laue lenses," Sci. Rep. **3**, 1307 (2013).
18. H. Kang, H. Yan, Y. Chu, S. Lee, J. Kim, E. Nazaretski, C. Kim, O. Seo, D. Noh, A. Macrander, G. Stephenson, and J. Maser, "Oxidation of PtNi nanoparticles studied by a scanning x-ray fluorescence microscope with multilayer Laue lenses," Nanoscale **5**(17), 7184–7187 (2013).
19. H. Yan, J. Maser, A. Macrander, Q. Shen, S. Vogt, G. Stephenson, and H. Kang, "Takagi-Taupin description of x-ray dynamical diffraction from diffractive optics with large numerical aperture," Phys. Rev. B **76**, 115438 (2007).
20. R. Conley, C. Liu, J. Qian, C. Kewish, A. Macrander, H. Yan, H. Kang, J. Maser, and G. Stephenson, "Wedged multilayer Laue lens," Rev. Sci. Instrum. **79**, 053104 (2008).
21. T. Koyama, T. Tsuji, H. Takano, Y. Kagoshima, S. Ichimaru, T. Ohchi, and H. Takenaka, "Development of multilayer Laue lenses; (2) circular type," in *10th International Conference on X-Ray Microscopy,* I. McNulty, C. Eyberger, and B. Lai, eds.,100-103, (Amer. Inst. Physics, Melville, 2011).
22. E. Nazaretski, J. Kim, H. Yan, K. Lauer, D. Eom, D. Shu, J. Maser, Z. Pesic, U. Wagner, C. Rau, and Y. S. Chu, "Performance and characterization of the prototype nm-scale spatial resolution scanning multilayer Laue lenses microscope," Rev. Sci. Instrum. **84**, 033701 (2013).
23. E. Nazaretski, K. Lauer, H. Yan, N. Bouet, J. Zhou, R. Conley, X. Huang, W. Xu, M. Lu, K. Gofron, S. Kalbfleisch, U. Wagner, C. Rau and Y. S. Chu, "Pushing the limits: an instrument for hard X-ray imaging below 20 nm," J. Synchrotron Rad. **22**, 336–341 (2015).
24. R. Conley, N. Bouet, J. Biancarosa, Q. Shen, L. Boas, J. Feraca, and L. Rosenbaum, "The NSLS-II multilayer Laue lens deposition system," Proc. SPIE **7448**, 74480U (2009).
25. H. Yan, H. C. Kang, J. Maser, A. T. Macrander, C. M. Kewish, C. Liu, R. Conley, and G. B. Stephenson, "Characterization of a multilayer Laue lens with imperfections," Nucl. Instr. Meth. Phys. Res. A **582**, 126–128 (2007).
26. E. Nazaretski, X. Huang, H. Yan, K. Lauer, R. Conley, N. Bouet, J. Zhou, W. Xu, D. Eom, D. Legnini, R. Harder, C.-H. Lin, Y.-S. Chen, Y. Hwu, and Y. S. Chu, "Design and performance of a scanning ptychography microscope," Rev. Sci. Instrum. **85**, 033707 (2014).
27. X. Llopart, R. Ballabriga, M. Campbell, L. Tlustos, and W. Wong, "Timepix, a 65k programmable pixel readout chip for arrival time," energy and/or photon counting measurements. Nucl. Instr. Meth. Phys. Res. A **581**, 485–494 (2007).
28. X. Huang, H. Yan, R. Harder, Y. Hwu, I. Robinson, and Y. Chu, "Optimization of overlap uniformness for ptychography," Opt. Express **22**(10), 12634–12644 (2014).
29. P. Thibault, M. Dierolf, A. Menzel, O. Bunk, C. David, and F. Pfeiffer, "High-resolution scanning X-ray diffraction microscopy," Science **321**, 379–382 (2008).

---

1. Introduction

Focusing hard x-rays close to atomic dimensions and studying complex systems at that length scale have been an ultimate goal for x-ray imaging. Multilayer Laue lenses (MLLs) [1] have emerged as optics capable of reaching that goal. They have demonstrated superior performance in focusing hard X-rays by overcoming one major obstacle encountered in the fabrication of diffractive optics: fabricating very fine structures with individual layer thickness on the order of a few nanometers yet with a high aspect ratio, which is the requirement for achieving a small focus with high efficiency particularly for hard X-rays [2, 3]. Since the concept was proposed [4], the MLL development has progressed from a miniature lens for conceptual demonstration

#233519 - $15.00 USD Received 29 Jan 2015; revised 27 Mar 2015; accepted 29 Mar 2015; published 4 May 2015

[5, 6] to a real focusing optic with a large aperture for imaging applications [7, 8]. Different material systems and deposition methods were explored for MLL fabrication [9, 10, 11, 12]. The fabrication of the circular geometry (sometimes referred as multilayer zone plate) was extensively explored as well [13, 14, 15]. Several X-ray imaging experiments using MLLs have been demonstrated [16, 17, 18], indicating that the optic is now mature enough for scientific applications. To date, most of the reported X-ray experiments were performed using MLLs that consist of flat zones. Though easier to fabricate, the flat-zone MLLs cannot focus efficiently to spot sizes much below 10 nm, owing to dynamical diffraction effects [19]. To obtain single-nanometer focus size and to achieve focusing efficiency above 50%, wedged MLLs with progressively tilted zones are required. Proof of concept growth of wedged MLLs in linear [20] or circular geometries [21] was reported previously, but they were targeted towards conceptual demonstrations with optical parameters not very desirable for science experiments.

Here we report the fabrication of a linear wedged MLL with an aperture size of 31 μm, an outermost zone-width of 2.8 nm and a focal length of 3.2 mm at an optimum operating energy of 14.6 keV, ready to be incorporated into an MLL microscope for scientific applications [22, 23] The lens has been fully characterized using scanning electron microscopy (SEM) analysis, rocking curve and ptychography measurements, for zone placement error, efficiency and focus wavefield characterization, respectively. Experimental data exhibit a good agreement with the theoretical calculations, indicating successful fabrication of a wedged MLL. To the best of our knowledge, this is the first linear wedged MLL reported with its performance fully characterized using X-rays, thereby representing a significant technological advancement toward new frontiers of X-ray nanofocusing.

2. Wedged MLL fabrication

For an incident plane wave, an ideally curved MLL consists of a set of confocal paraboloids [19], taking the form:

$$y_n^2 = n\lambda(f - z) + n^2\lambda^2/4, \tag{1}$$

where y_n is the position of the nth zone and z is the depth along the optical axis. At $\sim$1 $\mathring{A}$ X-ray wavelength, the second term is negligible, thus

$$y_n \approx a(z)\sqrt{n\lambda f}, a(z) = \sqrt{1 - z/f_s}, \tag{2}$$

Here, $a(z)$ serves as a scaling factor that shrinks the zone width along the depth z . Because the focal length of an MLL is linearly proportional to energy, while the tilting angle is a structural parameter that is fixed after growth, we use f_s as a structural focal length to distinguish it from the real focal length. When the lens thickness is significantly smaller than the structural focal length, f_s, this scaling factor is approximated to a linear gradient,

$$a(z) \approx 1 - \frac{z}{2f_s}. \tag{3}$$

Equations (2) and (3) leads to a wedged MLL with zones oriented in such a way that each zone is oblique to the optical axis, intersecting the optical axis at $2f_s$, as shown in Fig. 1.

As a result, the Bragg law is approximately satisfied across the whole aperture of the MLL,

$$2d\sin\theta = \lambda, \theta \approx y/2f_s, d \approx \lambda f/y, f_s = f. \tag{4}$$

Optimum focusing performance is then achieved. One may notice that the structural focal length, f_s, in Eq. (3), has to equal the real focal length in order to satisfy Bragg's law in Eq. (4). This requirement implies that the best performance of a wedged MLL is achieved only at the specific energy for which the particular MLL was designed.

#233519 - $15.00 USD Received 29 Jan 2015; revised 27 Mar 2015; accepted 29 Mar 2015; published 4 May 2015

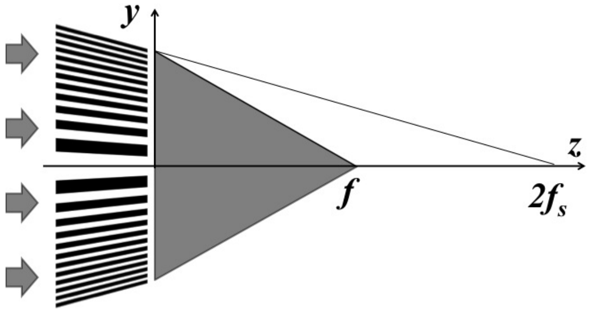

Fig. 1. A schematic drawing of the wedged MLL. Zones are titled to the incident beam progressively as they are positioned toward the outer region of the lens. The extension of the layers would intersect with the optical axis at $2f_s$. At the energy where the real focal length, f, equals to the structural focal length, f_s, optimum performance is achieved.

A wedged MLL imposes one significant challenge not encountered for tilted or flat MLL on the fabrication process: precise control of the thickness gradient in the lateral direction (corresponding to the z-direction in Fig. 1). In sputter deposition, this can be done by designing a special mask that regulates the atomic flux bombarding the substrate in the lateral direction, so the growth rate is position-dependent. Figure 2(a) is a schematic of the deposition setup. The mask used has five open windows. Their shapes are determined from the distribution of atomic flux density and the deposition thickness profile needed. The left- and right-most windows have a narrower opening toward the center. Therefore, the portion of the substrate closer to the center is exposed less to the atomic flux as it moves in and out. This compensates exactly for the non-uniform flux density in the horizontal direction, thereby resulting in a uniform film thickness. These two windows are used to generate MLLs with flat zones for reference. The center three windows are used to grow wedged MLLs on six substrates. Each of the three windows is designed to produce a triangular thickness gradient, where the gradient deposited on neighboring substrates switches sign. The opening is designed in such a way that the amount of material deposited on the substrate is linear in the horizontal direction. The flux density variation along this axis necessitates a slight curvature to the mask profile. Because the maximum flux density is larger at the center, the middle window is smaller than the other two in order to grow identical wedged MLLs on all six substrates. Figure 2(b) is a picture of the actual mask designed for four Silicon/Tungsten Silicide target pairs.

Using this mask and a dedicated deposition system [24], we deposited a wedged multilayer stack that consists of 7688 alternating Si and WSi_2 multilayers, corresponding to a 58% of the half MLL structure. A 2 mm-thick Si (100) wafer is used as the substrate, which is placed about 73 mm away from the magnetron sputter sources. Multilayer deposition was performed by alternatively raster-scanning the substrate in front of the fixed mask and cathode array in sequence. Only one sputtering source was energized at a time in order to deposit one complete layer. The mask as shown in Fig. 2(b) is inserted between the substrate and the magnetron guns to generate a gradient in the lateral deposition rate [20]. Four sputtering sources, two for each material, were utilized in order to reduce the effects of source depletion on the growth rate. All four sources were energized at a constant power of 350 W using an ION1500 DC sputtering power supply. The source to sample distance was approximately 70mm, and deposition was performed at a constant pressure of 4 mTorr and a 10% nitrogen/90% argon atmosphere. Figure 2(c) is a cross-section image stitched from 29 SEM pictures showing the deposition thickness variation along the lateral position, which exhibits good linearity between 3 mm and

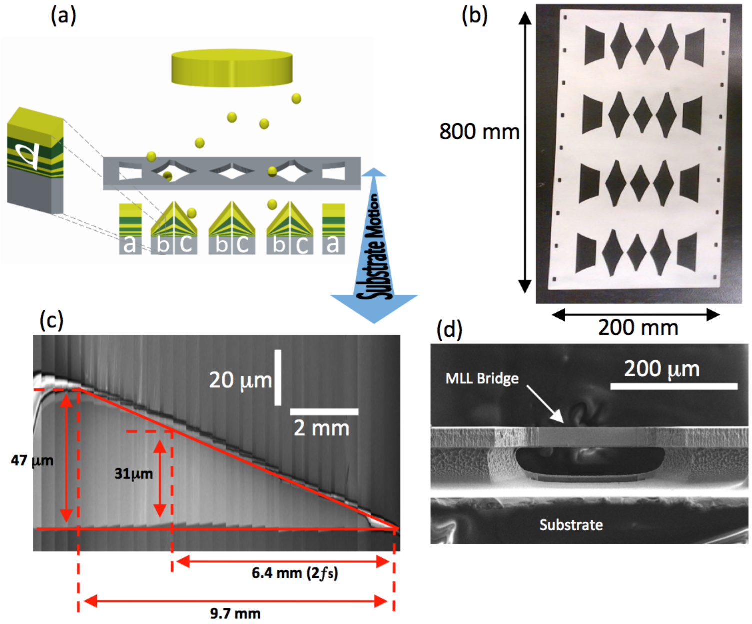

Fig. 2. (a) A schematic of the deposition setup. A profiled mask cut that produces a film gradient is inserted in-between the target and the substrate. Six sets of substrates labeled "b" and "c" would have identical wedging gradients, although in the reverse orientation. After the deposition, a small section (labeled "d") is cut from any of these wedged multilayer stacks to produce a wedged MLL. In order to simplify growth rate calibration with x-ray reflectivity measurements, short uniform thickness sections in the mask were cut to produce a uniform film thickness on substrates labeled "a". (b) A photograph of the fabricated mask used for four pairs of targets. It has a rectangular shape. The non-rectangular appearance is due to the viewing angle. (c) The cross-section of the multilayers after a completed growth. The wedged MLL was sectioned at a location, 6.4 mm away from the corner. (d) SEM image of the side view of the sectioned wedged MLL with 31 μm aperture size. The X-ray incident direction is perpendicular to the paper surface.

9 mm from the corner where the layer thickness is zero. This indicates that the mask works as expected. The total thickness deposited onto the substrate ranges from 0 to 47 μm across the span of substrate width. The multilayer stack was then sectioned using a combination of reactive ion etching and focused ion beam polishing, at a position of 6.4 mm away from the corner (Fig. 2(d)). Therefore, the lens aperture size is about 31 μm, and the structural focal length determined from the wedging is 3.2 mm. As discussed previously, the optimum performance is achieved only at the energy at which the lens true focal length is 3.2 mm. After sectioning, the wedged MLL is about 9.5 μm thick. The wedged MLL parameters are summarized in Table 1.

Table 1. Parameters for the wedged MLL measured in this experiment.

Number of layers	Outmost zone width	Aperture	Thickness	Focal length (14.6 keV)
7688	2.8 nm	31 μm	9.5 μm	3.2 mm

3. Performance characterization

The focusing performance of the lens is significantly affected by the zone placement error, which is the deviation of the zone position from the ideal value obeying zone plate law (Eq. (1)). A significant zone placement error can be introduced during the growth if the growth rate decay is not carefully calibrated and compensated. SEM provides a metrology tool that can accurately evaluate this error. According to Eq. (2), the position of the nth zone, y_n, holds a inear relationship with $\sqrt{n}$, and the slope is equal to $\sqrt{\lambda f}$. Any deviation from this linearity reflects growth imperfection of layer positions. Since the index, n, for a zone is deterministic, the insertion of marker layers (triple-wide or larger zones) which can be easily recognized in SEM, allows assessment of this linearity with an accuracy only limited by the SEM resolution. Figure 3(a) shows an SEM image with marker layers clearly observable. The slope of the linear fitting to y_n vs. $\sqrt{n}$ (Fig. 3(b)) is 0.522. Therefore, the optimum energy for this specific wedged MLL is at 14.6 keV, at which the focal length is 3.2 mm. The residual phase error from the linear fitting (inset of Fig. 3(b)) indicates the degree of imperfection of the lens across the aperture. Due to a noted lack of sufficient in-situ rate monitors [1], several deposition iterations are usually required to obtain diffraction-limited zone placement accuracy. This lens was produced without any iterative correction. Consequently, the associated phase error is sizable. The measured zone profile can be incorporated into the modeling approach to calculate its performance, discussed in further detail elsewhere [25].

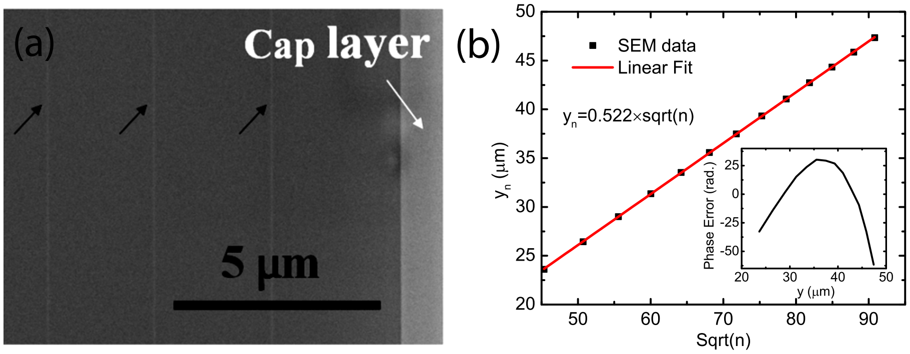

Fig. 3. (a) An SEM image showing 3 marker layers (pointed by black arrows). (b) A plot of the marker layer positions versus $\sqrt{n}$, where n is the zone index. A linear fit is also shown. The slope corresponds to $\sqrt{\lambda f}$. The inset shows the residual error from the linear fit, presented as the phase error associated with the zone placement error across the lens aperture. For an ideal lens it should be zero.

The superior performance of a wedged MLL is a consequence of wedging each zone to its proper angle. To understand its properties, it is very important to characterize the perfection of wedging. Although SEM analysis (Fig. 2(c)) clearly depicts a lateral thickness gradient, an x- ray measurement provides the ultimate characterization of the perfection of the wedged MLL. We performed two different types of x-ray characterizations. The first is a rocking curve measurement for efficiency, which was conducted at Beamline 1-BM at the Advanced Photon Source (APS) located at Argonne National Laboratory. In this measurement, the lens was illuminated by a monochromatic beam at 14.6 keV. A pixel array detector (Pilatus 100k), placed at 0.96 m downstream of the lens, was used to capture the far-field diffraction pattern as the lens is rotated. The pixel size of the Pilatus detector was 172 μm. Figure 4(a) shows two such far-field images, one taken at the angle favoring the negative first (focusing) order and the other at the angle favoring the positive first (diverging) order. Horizontal lines seen in the image cor-

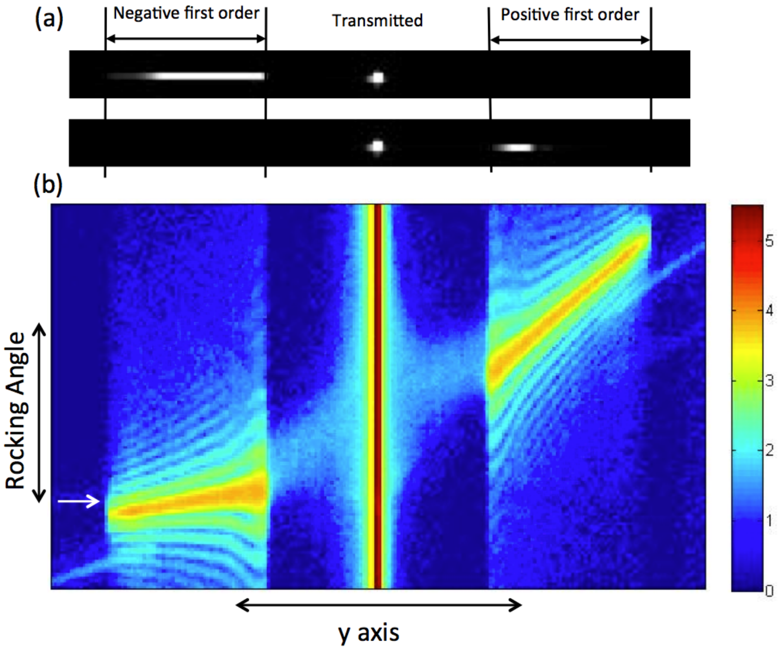

Fig. 4. (a) Far-field diffraction images taken at angles favoring the negative first (top) and positive first (bottom) orders. Vertical lines indicate the extent of each diffraction order on the far-field detector. Intensity is plotted on a linear scale. (b) Stacked line profiles obtained from (a) at different rocking angles. Intensity is plotted on a logarithmic scale. The white arrow shows the angular position at which optimum efficiency for focusing is achieved. The difference between the negative first and positive first orders is evident.

respond to the spread of the wavefront of the diffracted wave from the MLL on the detector. The length of the line is proportional to the numerical aperture (in other words the divergent angle) of the corresponding diffraction order. The longer and the more uniform the line is, the better for focusing. If we integrate the intensity vertically and stack line profiles at different angles together, a more interesting plot can be seen in Fig. 4(b), in which the focusing and diverging orders distinguish themselves very clearly. Because of the wedging, only at a specific angle (indicated by an arrow in Fig. 4(b)) the focusing order (left-hand side) has a very uniform diffraction intensity distribution, while away from it the intensity diminishes very quickly. The pattern is slightly tilted with respect to the horizontal axis and has a long spatial extent. The fringes were used to obtain the section thickness. This actually indicates the imperfection of this wedged MLL. For a perfect wedged MLL, this angle-dependent diffraction pattern of the focusing order should be well aligned with the horizontal axis so that a very high efficiency is achieved at a particular angle. On the other hand, the angular extent of the diffraction pattern of the diverging order is much larger. Conversely, at each angle its spatial extent is much narrower. This is due to the fact that the wedging adversely affects the diverging order; it suppresses the diffraction into a very narrow local region that moves along with the rocking angle. To be quantitative, we calculated efficiencies as a function of rocking angle from the integrated intensity within the spatial span of the negative first and positive first diffraction orders on the detector normalized to the total incident intensity of the central transmitted beam in the absence of the lens. In order to understand the effect of imperfection, we first studied the efficiencies of a corresponding perfect lens. Unlike an MLL with flat zones which has symmetric efficiency peaks for the focusing and diverging orders at two opposite angles, the wedged MLL shows a highly asymmetric diffraction pattern, favoring the focusing order at zero degree. Figure 5(a) is an efficiency simulation as a function of the incidence angle for two perfect MLLs with identical parameters (see Table 1), except that one has flat zones and the other has wedged zones. A dynamical diffraction formalism which includes up to the ±5th diffraction orders is applied in the simulation [19]. Phase functions of pseudo Fourier series, $\phi_h = h\pi y^2/(\lambda f)$ for flat-zone MLL, and $\phi_h = h\pi y^2/(\lambda f a(z)^2)$ for wedged MLL, are used in the calculation. Here h refers to the order of the diffraction considered in the formalism. As seen from the plot, for flat zones the efficiency is exactly symmetric with respect to the zero angle, at which angle the incident plane wave is parallel to the multilayer. The peak efficiency of about 11% is achieved at 0.22 degrees. The very low efficiency at zero degree is due to the strong dynamical effect at a large thickness of 9.5 μm at 12 keV. Unless the MLL is tilted and a Bragg condition is satisfied locally, a higher efficiency cannot be achieved. The wedged MLL, on the other hand, has an efficiency peak of the negative first order centered at zero degree. This is because the Bragg condition is mostly satisfied everywhere at this angle. The peak is substantially narrower as a result of strong dynamical diffraction effect. As compared to the flat-zone MLL, an almost five-fold increase of the peak efficiency is observed. The efficiency for the positive first order is significantly suppressed and is broadened.

Real lenses always have some imperfections. As such, the measured zone position profile obtained from SEM analysis (Fig. 3(b)) has to be incorporated in the theoretical model for accurate efficiency calculations. In this case, the corresponding phase function is changed to, $\phi_h = h\pi(1.889y + 8.553\times10^{-4}y^2 + 1.165\times10^{-5}y^3)/a(z)^2$. The polynomial is obtained by fitting the curve in Fig. 2(b). The comparison with the experimental data is depicted in Fig. 5(b). Highly asymmetric peaks clearly indicate that wedged zones are fabricated, and the good agreement between the theoretical calculation and experimental data verifies that the designed wedging is achieved. Due to the imperfection of zone placement, however, the measured efficiency of the focusing order is ∼27%, considerably lower than that for a perfect wedged MLL. To elucidate in which part of the lens the imperfections were most consequential, we plot in Fig. 5(c) and (d) the intensity variation of the focusing wavefield inside a perfect and a real wedged MLL with zone placement error as shown in Fig. 3(b), respectively. In a perfect lens, the wavefield only varies along the thickness direction and is a constant across the entire aperture. On the other hand, in the real lens with imperfection the wavefield decreases toward the outer region of the aperture where the zone width is the smallest. This variation is more pronounced at a large thickness, indicating that it is associated with dynamical diffraction effect. The presented zone placement error leads to a deviation from the Bragg condition. When it becomes significant the Bragg diffraction is no longer excited. Particularly in the region with thin zones and a large thickness, the tolerance to deviation from the Bragg condition is very small. Therefore the performance in this area is more sensitive to the error. The noticeable difference in peak width of the positive first order between the simulation and the measurement may be due to different types of imperfections. One possibility is bending or twisting of the lens, which is discussed later.

In addition to the efficiency, we also characterized the wavefield near the focus of the wedged MLL via ptychography experiment at an APS Beamline 34-ID-C. Details of the method and the experimental setup can be found elsewhere [8, 26]. A coherent and monochromatic beam at 14.6 keV was shaped to $6\times40\ \mu\text{m}^2$ by beam-defining slits to illuminate the MLL. A resolution test pattern (X500-200-16, Xradia Inc., now Zeiss) was scanned near the focal plane behind a rectangular (10×20 μm) gold order-sorting-aperture (OSA) with a 50 um-thickness. A Timepix pixel-array detector [27] with 512×512 pixels and 55 μm pixel size was placed 1 m away from the test pattern and was used to record the far- field diffraction pattern. The ptychography

#233519 - $15.00 USD Received 29 Jan 2015; revised 27 Mar 2015; accepted 29 Mar 2015; published 4 May 2015

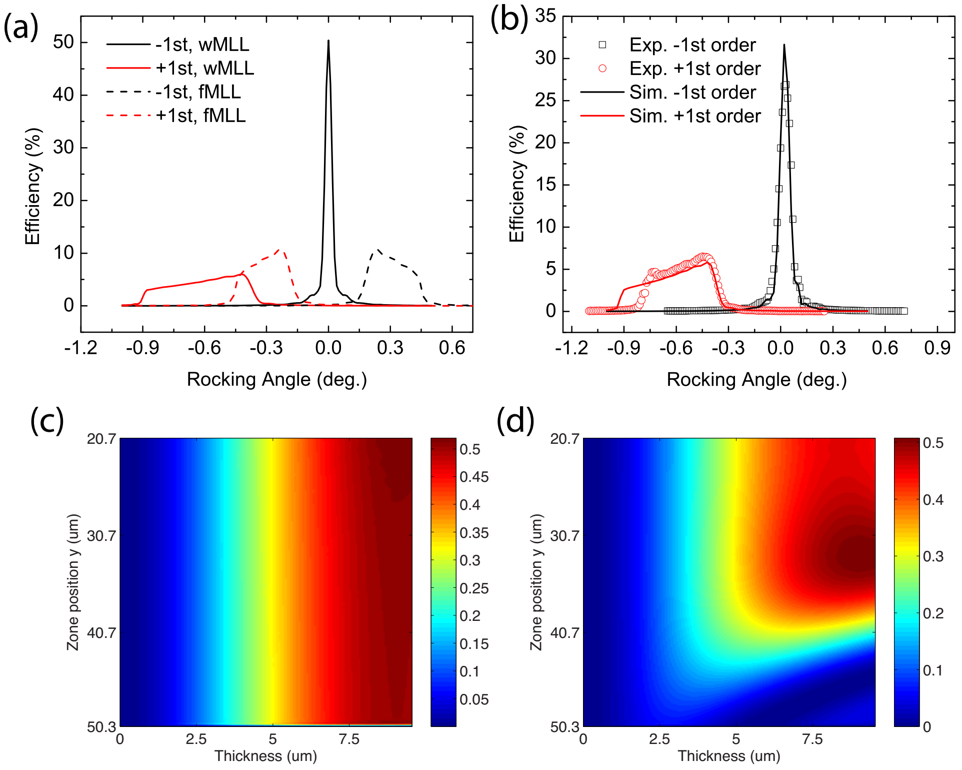

Fig. 5. (a) The simulated efficiencies of the negative first (focusing) and positive first (diverging) orders as a function of the rocking angle for MLLs with flat and wedged zones at 14.6 keV. Both lenses are perfect and have the same parameters shown in the following except the wedging: a thickness of 9.5 μm, an aperture size of 31 μm and an outmost zone width of 2.8 nm. For the wedged MLL, we assume that $f = f_s = 3.2$ mm at 14.6 keV. (b) The simulated efficiencies of the negative first (focusing) and positive first (diverging) orders compared with the experimental data. The measured zone placement error in Fig. 3(b) is incorporated into the theoretical calculation. (c) Intensity variation of the negative first order inside the perfect wedged MLL. In this case, the intensity is only a function of thickness, independent of the zone position. (d) A similar plot for a wedged MLL incorporating zone placement error is shown in Fig. 3(b). The diffraction intensity varies with both the thickness and the zone position. Particular at a large thickness, the intensity diminishes quickly in the outermost region where the zone width is the smallest. This change is due to the presence of the zone placement error.

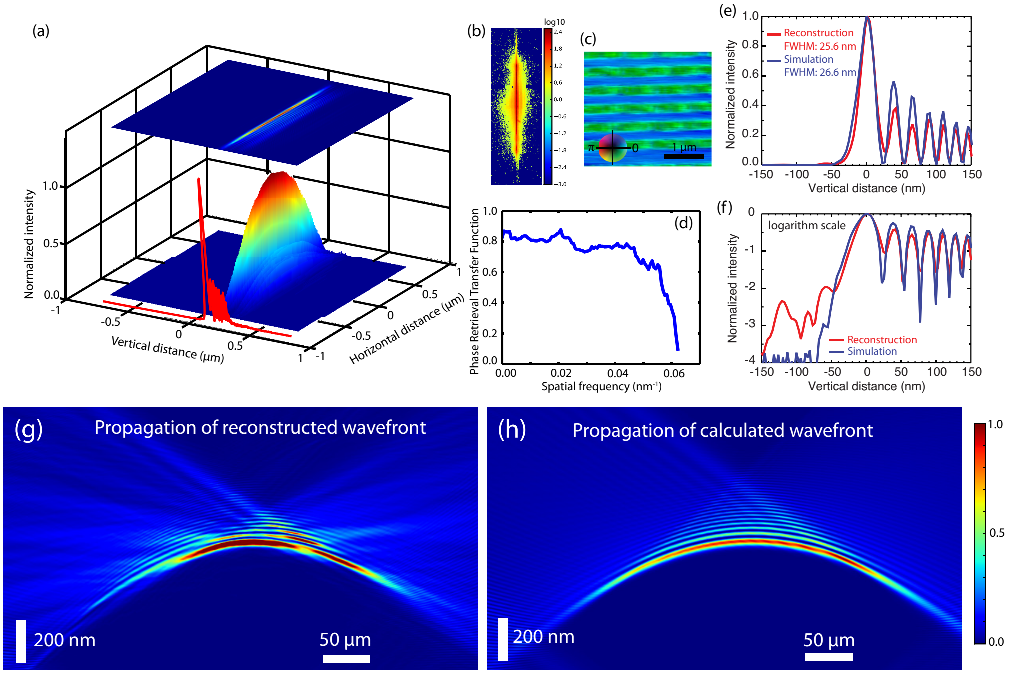

Fig. 6. (a) Isometric intensity plot of the X-ray wavefront at the focal plane. (b) A typical frame of collected diffraction data in logarithmic scale. (c) The reconstructed test sample image. (d) Phase retrieval transfer function of the reconstruction. (e) Intensity line profile through the focus. The experimentally determined focus size of 25.6 nm agrees well with simulated focus size of 26.6 nm. (f) Intensity line profile on the logarithmic scale. (g) and (h) are the wavefield intensity variations along the optical axis obtained from reconstruction and theoretical calculation, respectively.

scan covered a 3×3 μm^2 region with a constant radial scaling factor of 126 nm following a Fermat spiral trajectory [28], which provides an optimized overlap uniformity over the scanned area. A completed ptychography scan consists of 178 positions. At each scan position, the diffraction pattern is accumulated with 20 frames of 0.5 second exposure time. Each pixel located on the inter-module gaps was evenly split into 3 pixels (the central 4 pixels on the detector were divided into 3×3 pixel each). This modified dataset was used at the beginning of the reconstruction process, and the gap pixels were then allowed to be updated in following iterations. Direct beam leakage through the OSA was masked out, and a data array of 96×480 pixels was cropped to feed into 1000 iterations of Difference Map algorithm [29]. The initial probe was a Gaussian wave with a full-width-of-half-maximum (FWHM) of 100 nm, and the initial object was a complex random array. The reconstructed real-space pixel size is about 16×3 nm^2.

The isometric surface of the reconstructed wavefront intensity at the focal plane is shown in Fig. 6(a). A typical frame of diffraction pattern is shown in Fig. 6(b). Figure 6(c) is the reconstructed grating sample structure with brightness and color representing amplitude and phase, respectively. The intensity variation along the horizontal direction is caused by scattering from beam-defining slits placed 15 cm upstream of the lens [8]. A distortion on the focus due to the zone placement error was observed. The intensity line profile through the focus (Fig. 6(e)) shows a strong primary peak and considerable side lobes are visible on the right side. The primary peak exibits a FWHM width of 25.6 nm, when fitted by a Gaussian shape. As a com-

#233519 - $15.00 USD Received 29 Jan 2015; revised 27 Mar 2015; accepted 29 Mar 2015; published 4 May 2015

parison, we show the calculated wavefield intensity, taking into account zone displacement error obtained from SEM analysis. The measured focus profile displays excellent agreement with the calculated profile, which has a FWHM of 26.6 nm for the primary peak. Figure 6(f) shows the same curves on a logarithmic scale, where positions of satellite peak shows remarkable agreement. The slightly smaller FWHM width from the reconstruction could be due to various factors, such as an uncertainty in reconstruction and unaccounted phase effect in the theoretical calculation. Nevertheless, the difference is within the error bar of our analysis, which is ±1.2 nm. If the lens were perfect, it would have a diffraction-limited focus size of 10 nm. To understand how the wavefield propagates through the focus, we plot in Fig. 6(g) and (h) the reconstructed and calculated intensity distributions along the optical axis. All major features shown on the theoretical calculation are captured by the reconstruction, but with small differences.

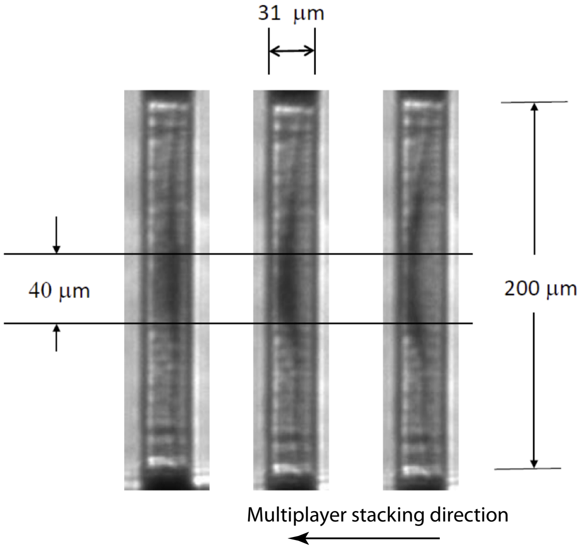

Fig. 7. Transmission images on a CCD at three successive rocking angles near the diffraction peak. Each of the three images is separated by 0.02 degrees. The dark band near the middle in each image occurs due to extinction since diffraction diverts the energy from the transmitted beam. Wedging widens the extinction band at the peak diffraction efficiency since a wider portion diffracts at the same rocking angle than would be the case for an MLL with parallel multilayer interfaces. If ideally wedged, the entire 31 μm -wide MLL aperture would show an extinction band. This work used a central 40 μm portion of wedged MLL, where the angular distortion is minimal. The X-ray beam direction is perpendicular to the paper surface.

We ascribe the observed small difference to other type of imperfections. In addition to the zone displacement error, accumulated film stress during deposition could degrade the interfacial quality and uniformity of the multilayers. Sectioning and polishing of the as-grown films, required for producing a usable MLL optic could also introduce structural deformation, nearly impossible to model. Furthermore, evidence of some bending or twisting of MLL layers has been observed on the investigated wedged MLL. Transmission x-ray images in Fig. 7 exhibits this effect. Here an optically-coupled CCD camera (Andor Neo, 6 μm pixels size) with a scintillation screen using a 2.5x objective lens was used to image the transmitted beam 0.33 m downstream. When the wedged MLL is tilted to a specific angle relative to the incident x-ray beam, the zones satisfying the Bragg condition strongly diffracts X-rays, resulting in a dark extinction band in the transmission image since a fraction of energy is diverted into the diffraction channel [1]. If the lens had no angular distortion, the extinction band would be parallel to the multilayers and vertically straight in Fig. 7. For an ideally wedged MLL with no angular distortion, the extinction band would show up over the entire 31 μm MLL aperture, since all zones satisfy the Bragg condition simultaneously. The observed narrow and wavy extinction band indicates that the investigated MLL contains both zone placement errors and angular distortion. A possible cause of the latter is the over milling during FIB process, which results in a bridge structure without any substrate support underneath (see Fig. 2(d)). This work has been performed over the central region of the wedged MLL within the straight extinction band, where the angular distortion is minimal. These various defects exhibit interesting signatures in the MLL focusing behavior, however they are less important for the investigated wedged MLL reported here, since its focusing performance is accurately described by the zone placement error, which as shown above is most consequential for thin zones. Nevertheless, efforts are ongoing to optimize FIB parameters to minimize the structural distortion.

4. Summary

In summary, we report the first x-ray performance measurement on a wedged MLL. We present experimental evidence of successfully producing a wedged MLL with 31 μm aperture, 2.8 nm outermost zone width and a corresponding focal length of 3.2 mm at a photon energy of 14.6 keV. The rocking curve measurements confirm the characteristic diffraction attributes of a wedged MLL with a focusing efficiency of 27% at 14.6 keV, very close to the theoretical value of 32%. The focus size, determined by ptychography measurements, is 25.6 nm$\pm$1.2 nm, in excellent agreement with the calculation taking into account of measured zone placement error of the fabricated wedged MLL. In addition, the reconstructed wavefronts through the focus and focus profile are accurately described by the known zone placement error of the wedged MLL. On-going refinement on more accurate control of both the wedging and zone placement error is expected to yield more perfect wedged multilayer structures, capable of producing a smaller focal spot with higher efficiency. We anticipate that this powerful new focusing optic will open new and exciting opportunities for the study of materials, devices, biological and environmental systems using high-resolution hard X-ray microscopy.

Acknowledgments

We acknowledge the assistance of Michael Wojcik, Adam Kubec, Ralu Divan and Mark Erdmann in portions of this work. Work carried out at National Synchrotron Light Source II and the Center for Functional Nanomaterials at Brookhaven was supported by the Department of Energy, Office of Basic Energy Sciences under contract DE-SC00112704. I.K.R. is supported by the ERC “nanosculpture” advanced grant 227711. The measurements were carried out at APS beamline 1-BM-B and 34-ID-C operated by the US Department of Energy, Office of Basic Energy Sciences, under contract no. DE-AC0206CH11357. Beamline 34-ID-C was built with US National Science Foundation grant DMR-9724294.

#233519 - $15.00 USD Received 29 Jan 2015; revised 27 Mar 2015; accepted 29 Mar 2015; published 4 May 2015